



# An analysis of evaporative self-assembly of micro particles in printed picoliter suspension droplets

Sun Choi <sup>a,b,\*</sup>, Albert P. Pisano <sup>a,b,c</sup>, Tarek I. Zohdi <sup>b</sup>

<sup>a</sup> Berkeley Sensor and Actuator Center (BSAC), University of California at Berkeley, Berkeley, CA 94720, USA

<sup>b</sup> Department of Mechanical Engineering, University of California at Berkeley, Berkeley, CA 94720, USA

<sup>c</sup> Department of Electrical Engineering and Computer Science, University of California at Berkeley, Berkeley, CA 94720, USA

## ARTICLE INFO

### Article history:

Received 21 September 2012

Received in revised form 11 April 2013

Accepted 12 April 2013

Available online 26 April 2013

### Keywords:

Evaporative self-assembly

Non-equilibrium assembly

Micro particle

Picoliter droplets

Particle simulation

## ABSTRACT

We report systematic experimental and computational studies to analyze evaporative self-assembly of micro particles in printed picoliter suspension droplets. Evaporative self-assembly of micro particles in picoliter droplets is enabled by a droplet-printing system for small-scale particle suspension droplets. Experiments were performed to study the regime where particle interactive forces become comparable to hydrodynamic, evaporative forces of an evaporating droplet. A particle-based computational method was developed to calculate the particle-to-particle clustering time. In this study, we verify that there is a time-scale competition between particle-to-particle clustering and evaporation of the liquid medium that determines the final morphology of micro particle assemblies.

© 2013 Elsevier B.V. All rights reserved.

## 1. Introduction

Evaporative self-assembly of solid-phase materials in a liquid medium has numerous engineering applications, especially, in droplet printing technologies [1–3]. Experimentally, the evaporative self-assemblies of various geometrically-shaped solid materials were demonstrated at millimeter to nanometer scales in previous reports [4–7]. Although a number of experimental works [1,8–18] demonstrate precise control or patterning of 1 D, 2 D self-assembly of micro-scale colloids, due to the complexity of three-phase (liquid, solids and gas) systems, it is still challenging to analyze and model the dynamics of evaporative self-assembly from a theoretical standpoint. In particular, if one considers the significant ongoing effort in obtaining a high-level understanding of the equilibrium-state and crystallization processes of nanoparticle or proteins [6,7,19–28], there exist very few studies [5,15,29–31] on evaporative-assembly of micro particles. In those studies, it was claimed that the evaporative self-assembly of micro particles in equilibrium is driven by the meniscus effect of the evaporating, particle-carrier medium. However, non-equilibrium evaporative self-assembly of microparticles was not studied in-depth. In this article, we report experimental and computational studies to describe non-equilibrium evaporative self-assembly of micro particles in printed picoliter droplets. Experimentally, evaporative self-assembly of micro

particles in picoliter droplets was observed with a particle-suspension droplet-printing system. An experimental apparatus was developed to study the regime where particle interactive forces become comparable to hydrodynamic, evaporative forces of an evaporating droplet [16]. The system was used to observe evaporative self-assembly of particles in printed picoliter droplets and evaporation time of the droplets was measured by real-time observation. Along with the experimental work, a particle-based computational method [32–36] was modified to calculate particle clustering time in picoliter suspension of droplets. Experimental and computational analysis showed the importance of time-scale – “competition” – between particle-to-particle interactions and evaporation of a liquid medium, to determine the final morphology of micro particle assemblies.

## 2. Experimental methods

### 2.1. Materials

A liquid suspension of silica microspheres (Silicon dioxide-based micro particles; diameter, 1, 3, and 5  $\mu\text{m}$ ; water, 95 wt.%; silica: 5 wt.%, Sigma-Aldrich) and a liquid suspension of fluorescent microspheres (Fluoresbrite Carboxylate<sup>R</sup>; diameter, 0.5  $\mu\text{m}$ ; excitation wavelength maxima: 360 nm, 441 nm, 529 nm, 641 nm; water, 97.5 wt.%; polystyrene microspheres: 2.5 wt.%, Polysciences, Inc.) was diluted into various concentrations of suspension (1.25, 0.625, and 0.3125 wt.% solutes). A liquid suspension of gold nanoparticles (diameter, 100 nm; water, 99.995 wt.%, Au,  $5 \times 10^{-3}$  wt.%; Nanopartz) was diluted into various concentrations of suspension ( $5 \times 10^{-4}$  wt.%,  $5 \times 10^{-5}$  wt.%, Au

\* Corresponding author at: Earth Sciences Division, Lawrence Berkeley National Laboratory (LBNL), University of California at Berkeley, Berkeley, CA 94720, USA. Tel.: +1 510 495 2658; fax: +1 510 643 6637.

E-mail address: [SChoi@lbl.gov](mailto:SChoi@lbl.gov) (S. Choi).

nanoparticles) and also was concentrated 10 times ( $5 \times 10^{-2}$  wt.%, Au nanoparticles) by using centrifugal separation of particles and medium and extracting a controlled volume of the medium above the particle layer at the bottom of a tube.

## 2.2. Fabrication of the printing heads

A 6 inch-Silicon-on-Insulator (SOI) wafer (top device layer: silicon 100 nm, buried oxide layer: silicon dioxide 400 nm, base: silicon 650  $\mu\text{m}$ , SOITEC, France) was used for the fabrication of the printing head. The backside of the SOI wafer was grinded by 400  $\mu\text{m}$  to reach the final thickness of 250  $\mu\text{m}$  and polished. Low-stress silicon nitride film of 35 nm was deposited on both sides of the wafer by Low-Pressure Chemical Vapor Deposition (LPCVD) for generating masking materials of wet-etching process. Then, back-side of the wafer was spin-coated with photoresist and baked at 120 °C for 5 min and placed in Buffered-Oxide-Etcher (BOE, BHF: DI water = 10:1) for 10 h to etch the silicon nitride layer of top-side of the wafer. After complete etching of the silicon nitride layer on the top-side, the photoresist was removed by photoresist removal (PRS-3000, J.T. Baker, USA) overnight. The wafer was diced into 1 cm  $\times$  1 cm dies and both top and back sides of each die were coated with photoresist. Photolithography was performed on top-side to define holes for a porous membrane of the printing head and Reactive-Ion Etching to etch top side silicon through the defined photo-patterns was followed by taking advantage of buried oxide as an etch-stop layer. After the removal of the photoresist, the top and backsides of the chip were coated with photoresist and reservoir area of the bulk suspension was defined by photolithography followed by RIE etching to open area for silicon wet-etching. Before wet-etching of bulk silicon layer, top-layer was coated with 10  $\mu\text{m}$ -thickness protective polymer (ProTEK B3, Brewer science, USA) to protect porous membrane structures on top-side from being etched by wet-etchant. The prepared chips are wet-etched for 4 h in the bath where 15 L of 5% Tetramethylammonium hydroxide (TMAH) solution was prepared at 90 °C. After wet etching is completed, the protective polymer was removed by PRS-3000/IPA/water rinse and BOE etching (5:1 BHF, 5 min at room temperature) was followed to etch a buried oxide layer completely. By design, thin, microporous membrane is released where the area of the membrane is 2 mm  $\times$  2 mm. The membrane side of the fabricated devices was treated by oxygen plasma (300 W, 250 mTorr, 1 min) to eliminate possible residue of protective polymer and the devices were placed on hot plate at 120 °C overnight to neutralize charge state of the membrane surface from hydrophilic state. Finally, the fabricated printing heads were coated with Fluorooctatrchlorosilane (FOTS) monolayer by Metal-Organic Chemical Vapour Deposition (MOCVD) to maintain the top side of membrane hydrophobic.

## 2.3. Fabrication of the handling wafer

A 4 inch-silicon wafer (Lightly p-type doped, Thickness: silicon 500  $\mu\text{m}$ ) was used for the fabrication of the handling wafer. Low-stress silicon nitride film of 35 nm was deposited on both sides of the wafer by Low-Pressure Chemical Vapor Deposition (LPCVD) for generating masking materials of wet-etching process. Top side of the wafer was coated with photoresist. Photolithography was performed on top-side to define a wafer-through hole (6 mm  $\times$  6 mm square) and Reactive-Ion Etching of silicon nitride layer through the defined photo-patterns was followed to define etching area. The wafer is wet-etched for 16 h in the bath where 15 L of 5% Tetramethylammonium hydroxide (TMAH) solution was prepared at 90 °C. After wet etching is completed, the protective polymer was removed by PRS-3000/IPA/water rinse and the surface of the wafer was cleaned by oxygen plasma (300 W, 250 mTorr, 1 min) to eliminate the residue of the protective polymer.

## 2.4. Fabrication of the printing head–handling wafer complex

A fabricated handling wafer was spincoated with photoresist. The printing head is placed on the center of handling wafer in a way that the membrane of the printing head is exposed to air without any blocking. Then, the printing head–the handling wafer with photoresist complex are baked together at 120 °C for 1 min on hot plate with heavy load press to promote the adhesion between the printing head and the handling wafer.

## 2.5. Experimental observation of evaporative self-assembly of particles

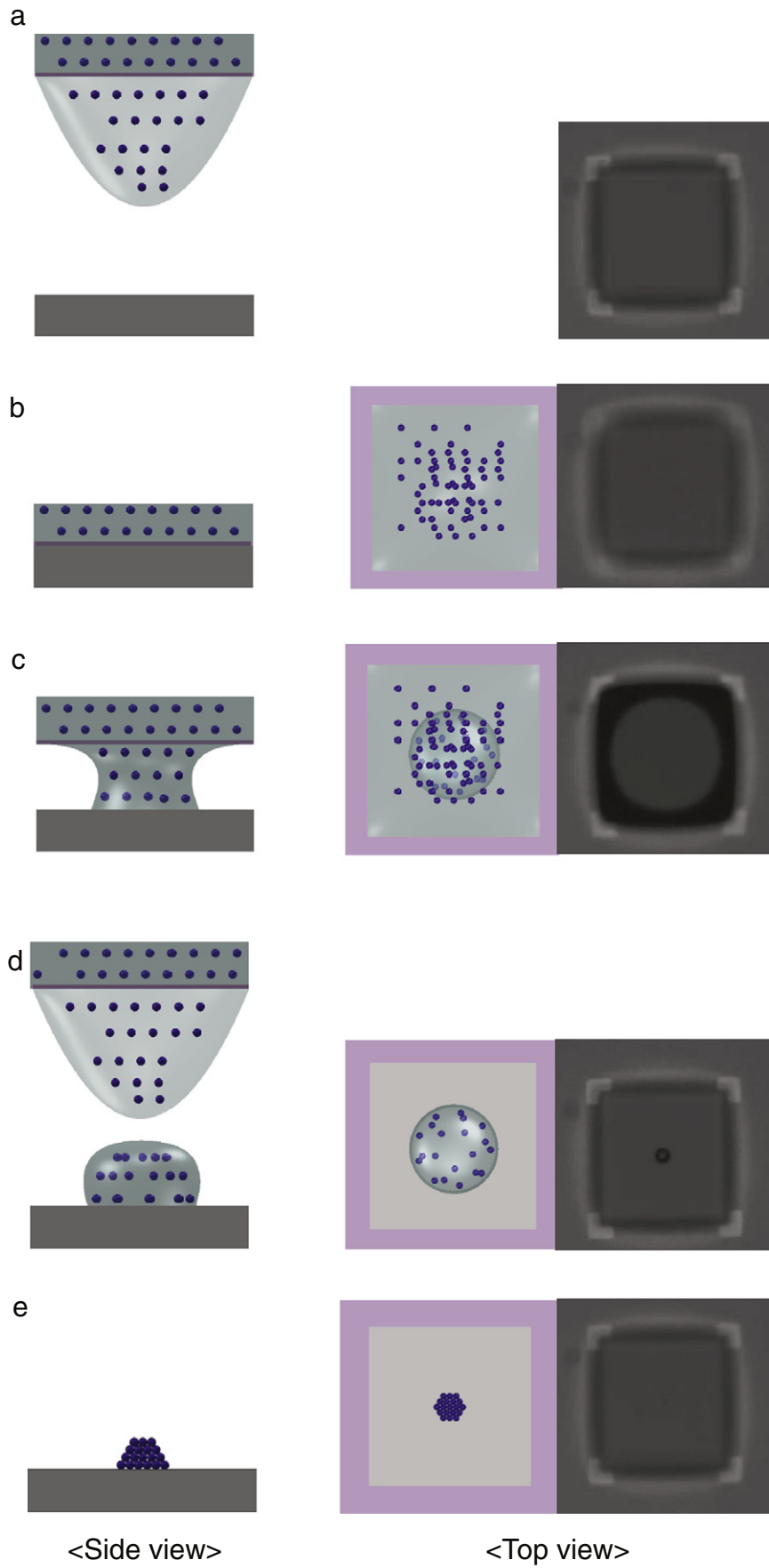
A printing head–handling wafer complex was attached to a mask holder of UV-exposure system for contact-photolithography (MA/BA6, Suss MicroTec, Germany) via vacuum. The mask holder was inserted to the system and a substrate for printing was loaded to this stage. After loading the substrate, the alignment of the printing head to the patterns on the substrate wafer was performed and the spacing gap between the printing head and the substrate was controlled and placed by the electronics of the system. The minimum threshold gap was a half of the width of pore size of the membrane. The micro, nanoparticle suspension was loaded to the reservoir of the printing head. Initially, 10  $\mu\text{L}$  volume of the suspension was loaded by micropipette to the reservoir forming a circular contact line of an overflowed droplet on top of the fluid-cell. The meniscus of the suspension was then flattened by drawing excessive volume of the suspension to ensure that two-dimensional symmetry of the meniscus surface was not perturbed. A thin, glass cover-slide was capped on the mask holder to prevent the evaporation of the suspension during printing. The contact of the printing head membrane was performed by driving the mask holder to the substrate. After 1 s of the contact, the head was driven back to the original position and the evaporation of the printed droplets were observed in-real time by optical microscope (5x magnification, UMPlanFI, OLYMPUS) in the printing system when the concentration of the suspension was sufficiently low to be transparent. Light intensity of microscope-light source was measured by light meter (EA<sup>TM</sup>33, EXTECH instrument) and it was 2.06 lux (= 3.01 mW/m<sup>2</sup>) and evaporative power of the droplet was calculated by

$$\frac{(\text{Latent heat of water at given mass of droplet})}{(\text{Contacting surface area of droplet})} = \frac{334 \left(\frac{\text{kJ}}{\text{kg}}\right) \times 200(\text{pg})}{200 \times 200(\mu\text{m}^2)}$$

$$= 1.67 \left(\frac{\text{W}}{\text{m}^2}\right),$$

which is 500 times stronger than the light intensity, so it was assumed that radiative power is negligible during the evaporation of the droplet. After the evaporation of the droplets was completed, the substrate with printed patterns was unloaded. Also, for the detailed analysis, close views of samples were imaged by field emission scanning electron microscopy (LEO 1550, ZEISS) in in-lens mode at operating voltage, 1.5 keV.

Fig. 1 shows the assembly method of micro particles in this study. Previously, it was observed that evaporative self-assembly of micro, nanoparticles in the picoliter droplets drives complete clustering of the particles prior to the completion of liquid medium-evaporation [16]. This unique evaporating characteristic of picoliter droplets on a hydrophobic surface motivates thorough examination of the regime where particle clustering rate is comparable to the evaporative rate of the liquid medium. In this work, a number of combinatorial sets of materials and concentrations of particle suspensions were used, to study the kinetics of evaporative self-assembly in the regime where particle effects become comparable to hydrodynamic effect of the liquid medium.  $5 \times 10^{-6}$ ,  $5 \times 10^{-5}$ ,  $5 \times 10^{-4}$ ,  $5 \times 10^{-3}$ ,  $5 \times 10^{-2}$  wt.% Au nanoparticle (diameter: 100 nm) suspension, 0.34, 0.68, 1.35, 2.70 wt.% polystyrene (PS) micro particle (diameter:



500 nm) suspension, 1, 5 wt.% silica micro particle (diameter: 1  $\mu\text{m}$ ) suspension were used for experimental and computational studies. Evaporation of picoliter droplets of micro particle suspension on a hydrophobic surface was monitored by optical microscope (5x magnification, UMPlanFI, OLYMPUS) in the system. High optical transparency of a thin membrane of the printing head and low-concentration suspensions allowed the observation of the convective motion of particles. Video clips for pinch-off and evaporation of picoliter droplets of 0.005 wt.% Au nanoparticle suspension was recorded to obtain the evaporation time of the droplets. It was assumed that the evaporation time of the droplet does not vary with the particle concentration in low particle volume fraction, because the viscosity does not change significantly [37]. The evaporation time of the same volume, picoliter droplets is assumed to be constant throughout all materials and all concentrations of the suspension in this study.

### 3. Particle-based computational modeling and calculation

Previously, numerous multi-phase flow phenomena, such as natural deposition of particles [7,16,38–42] or controlled-convective assembly [5,14,15,43–49] of the particles in evaporative flows, were interpreted by conventional hydrodynamic models. Assuming that the particles in evaporative flows behave as continuum species in the fluid, the motion of the particles are presumed to coincide with the streamlines of the fluid flow, and only the ‘fluid’ part of particulate flow was considered in the modeling. Although the global morphologies of particle-deposits were simulated by these ‘fluid’-based approaches [14,38,39,41–43,50], micro-scopic views of particle clustering behaviors were rarely discussed because particle-to-particle interactions are neglected in the analysis. Particle-to-particle, particle-to-solid or particle-to-fluid interactions are driven by electrostatic forces, mass-based forces or surface-based forces [36]. Obviously, those forces exist in evaporative self-assembly and are coupled with the evaporative flows, however, they were not incorporated in conventional hydrodynamic models. Particle-to-particle interactions generally occur by non-continuous, discrete events and continuous function-based mathematical models in the hydrodynamic models are not capable of interpreting those events. Also, free energy-based approaches are usually used for simulations of protein crystallization. However, parameters for the simulation, such as free energy, density fluctuation and chemical potentials are very difficult to be obtained in the modeling of non-equilibrium evaporative self-assembly. Recently, for the simulation of drying behavior of very small nanoparticles (diameter: <5 nm), a coarse-grain model was introduced to simulate the morphologies of nanoparticle assemblies by introducing particle-to-particle, particle-to-solid, particle-to-medium interaction factors [6,20,23,27]. This particle-based approach demonstrated accurate modeling of drying behaviors of very small nanoparticle assemblies in a very small area (<10  $\mu\text{m} \times 10 \mu\text{m}$ ), however, the range of the particle sizes and the area of modeling domains cannot be extended to macro-, micro-scales due to the computational limits. Also, the drag effect is exerted by surrounding fluids to the particles, however, it was not considered in the analysis. The accuracy can be substantially degraded if this model is used for macro-, micro-particle simulations. All the previous approaches, hydrodynamic-, free energy-based and a coarse-grain-modeling methods, were used to present either ‘fluid’-based or ‘particle’-based views of evaporative self-assembly, however, none of them is suitable for the simulation of the assembly of micro particles in picoliter suspension droplets. In order to develop insights into the phenomena, it is crucial to implement adequate computational methods for interpretation.

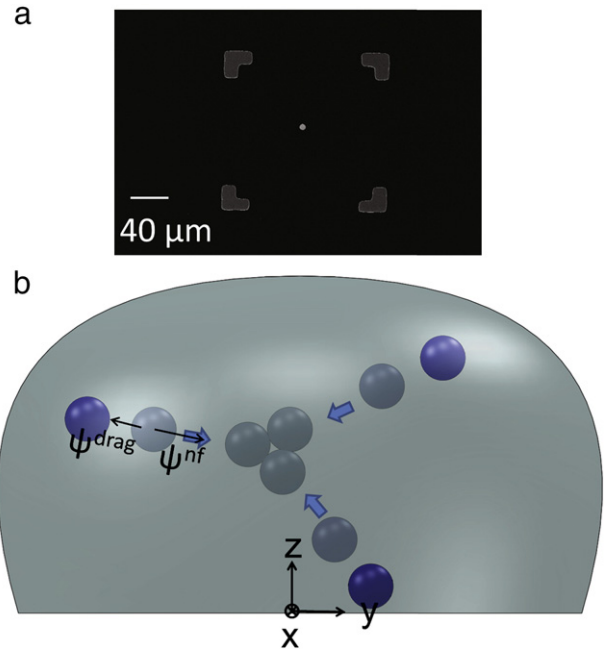


**Fig. 2.** a. SEM views of gold nanoparticle clusters (diameter: 100 nm). (i) A centered gold nanoparticle cluster with respect to gold alignment marks. The marks indicate the location of the initial contact line of the droplet. (ii) An analyzed image of alignment mark with a reference coordinate system of the computational work.

A particle-based computational model was developed to simulate the assembly behaviors of micro-, macro-scale particles in surrounding fluids during the evaporative self-assembly. By adding fluid-drag effect to the governing equations as described in Zohdi's work [36], Newton's 2nd law of motion was implemented to each single particle. The governing equation is

$$m_i \ddot{r}_i + c_i \dot{r}_i = \psi_i^{tot} = \psi_i^{int} + \psi_i^{ext} \quad (1)$$

where  $r_i$  is the position vector of the  $i^{th}$  particle,  $m_i$  is the mass of a single particle,  $c_i$  is a drag coefficient applied on the  $i^{th}$  particle and  $\psi_i^{tot}$  is the sum of the forces acting on the  $i^{th}$  particle, due to other particles in the system. The reference coordinate system is shown in Fig. 2.

In our systems, it was assumed that

$$\psi_i^{ext} = 0 \quad (2)$$

$$\psi_i^{int} = \psi_i^{nf} + \psi_i^{con} + \psi_i^{fric}, \quad (3)$$

where  $\psi_i^{nf}$  is the force due to near-field interaction,  $\psi_i^{con}$  is normal contact impulsive forces, and  $\psi_i^{fric}$  is frictional impulse forces. For  $\psi_i^{nf}$ , empirically-generated interaction laws for complex particulate ion-ion interaction are used to express attractive and repulsive components. A general form of  $\psi_i^{nf}$  is

$$\psi_i^{nf} = \sum_{j \neq i}^{N_p} \left( \alpha_{1ij} \|r_i - r_j\|^{-\beta_1} - \alpha_{2ij} \|r_i - r_j\|^{-\beta_2} \right) n_{ij} \quad (4)$$

where the  $\alpha$  and  $\beta$  are empirical material parameters. Particle-to-particle interactions are difficult to be quantified because the potential changes with material properties or experimental conditions. In

**Fig. 1.** Schematic of the printing procedure. Right column images of top view are corresponding optical snapshots of evaporating droplets. a. Particle suspension menisci are extruded to the upfront end of the membrane by gravity. b. Contact of the head with the substrate is achieved. c. Surface tension of the substrate attracts a fraction of the suspension fluid. d. Picoliter droplets are transferred to the substrate via pinch-off processes. e. Evaporative self-assembly of the particles forms 3-D clusters. The size of pore is 200  $\times$  200 ( $\mu\text{m}^2$ ). 5  $\times 10^{-3}$  wt.% gold nanoparticle suspension was used.

this work, it was assumed that an attractive interaction among particles is generated by both hydrodynamic effect of a drying droplet and van der Waals forces and it is expressed as a polynomial potential,

$$\psi_i^{nf} = \sum_{j \neq i}^{N_p} \left( \alpha_{1ij} \|r_i - r_j\|^{-\beta_1} \right) n_{ij} .$$

In this work, the first-order approximation of the equations was applied to comply with the computational model with the first-order approximation. Simplified attractive interaction force,  $\psi_i^{nf, att.}$  is

$$\sum_{j \neq i}^{N_p} \left( \alpha_{1ij} \|r_i - r_j\|^{-1} \right) n_{ij} .$$

A repulsive interaction among particles is generated by both a long-range, electrostatic interaction and a short-range, elastic interaction. A long-range, electrostatic repulsive interaction among particles was assumed to be generated by Yukawa repulsion [51]. Yukawa repulsion potential function,  $E_Y(r)$ , is  $\frac{\gamma}{r} \exp(-zr)$ , where  $\gamma > 0$  is the energy (coupling) parameter that characterizes the magnitude of repulsion while parameter  $z$  controls the decay of repulsive interaction. The corresponding electrostatic repulsive force,  $-\frac{dE_Y}{dr}$ , is expressed as  $\gamma(z-1-\frac{1}{z})(\frac{1}{r})$  after the first-order approximation of Taylor expansion and eliminating constant term to comply

with the proposed repulsive model,  $\psi_i^{nf} = \sum_{j \neq i}^{N_p} \left( \alpha_{2ij} \|r_i - r_j\|^{-\beta_1} \right) n_{ij}$ ,

from Eq. (4). A short-range repulsion was assumed to be generated by stored elastic energy of interpenetrated two particles,  $E_e, \frac{1}{2}kh^{3/2}$ , where the coefficient  $k$  is defined as  $k = \frac{4\sqrt{2}}{15} \frac{E}{1-\sigma^2} \sqrt{d}$ .  $E, \sigma$ , and  $d$  are Young's modulus, Poisson's coefficient, and the radius of the particle, respectively [33]. The corresponding elastic repulsive force,  $-\frac{dE_e}{dh}$ , is  $-\frac{5}{4}kh^{3/2}$ . This repulsive interaction force operates when  $h = \|r_i - r_j\| \leq d$ , by definition. On the other hand, the attractive interaction potential,

$$\sum_{j \neq i}^{N_p} \left( \alpha_{1ij} \|r_i - r_j\|^{-1} \right) n_{ij} ,$$

operates when  $h = \|r_i - r_j\| \geq d$ . It is very crucial to note that  $\psi_i^{nf}$  takes account not only inter-particle interaction forces but also the hydrodynamic effects. In other words, all factors to drive the clustering of particles were integrated into one source term,  $\psi_i^{nf}$ . A final form of  $\psi_i^{nf}$  is

$$\begin{aligned} \psi_i^{nf} &= \sum_{j \neq i}^{N_p} \left( \alpha_{1ij} \|r_i - r_j\|^{-1} - \gamma_{ij} \left( z_{ij} - 1 - \frac{1}{z_{ij}} \right) \|r_i - r_j\|^{-1} \right) n_{ij} \\ &= \sum_{j \neq i}^{N_p} \left( \alpha_{1ij} \|r_i - r_j\|^{-1} \right) n_{ij} \quad (d \leq \|r_i - r_j\|) \\ \psi_i^{nf} &= - \sum_{j \neq i}^{N_p} \left( \frac{5}{4} k \|r_i - r_j\|^{\frac{3}{2}} \right) n_{ij} = \sum_{j \neq i}^{N_p} \left( \alpha_{1ij} \|r_i - r_j\|^{-1} \right) n_{ij} \quad (d \geq \|r_i - r_j\|) \end{aligned} \tag{5}$$

In our system, it was assumed that

$$\psi_i^{con} = 0 \tag{6}$$

$$\psi_i^{fric} = 0 \tag{7}$$

because contribution of contact force is included in a repulsion interaction and contribution of friction force is negligible.

The governing equation can be solved recursively by recasting the relation as

$$r_i^{L+1,K} = G(r_i^{L+1,K-1}) + R_i \tag{8}$$

where  $K = 1,2,3,\dots$  is the index of iteration within time step  $L + 1$  and  $R_i$  is a remainder term that does not depend on the solution, i.e.

$$R_i \neq R_i(r_1^{L+1}, r_2^{L+1} \dots r_N^{L+1}) \tag{9}$$

The position of  $i^{th}$  particle was implicitly expressed as(10)

$$r_i^{L+1,K} = r_i^L + \underbrace{\frac{1}{1 + \frac{\Delta t}{m_i} \left( \frac{1}{2} \rho v_i^L C_{D,A} \right) \phi} (v_i^L \Delta t + \frac{\phi(\Delta t)^2}{m_i} (1-\phi) \psi_i^{nf,L})}_{\kappa} + \underbrace{\frac{1}{1 + \frac{\Delta t}{m_i} \left( \frac{1}{2} \rho v_i^L C_{D,A} \right) \phi} \left( \frac{\phi(\Delta t)^2}{m_i} \psi_i^{nf,L+1} \right)}_{G(r_i^{L+1,K-1})} \tag{10}$$

where

$$\psi_i^{nf,L} = \psi_i^{nf,L} (r_1^L, r_2^L \dots r_N^L) \tag{11}$$

and

$$\psi_i^{nf,L+1,K-1} = \psi_i^{nf,L+1,K-1} (r_1^{L+1,K-1}, r_2^{L+1,K-1} \dots r_N^{L+1,K-1}) \tag{12}$$

As discussed previously, only one variable,  $\alpha$ , reflects all interactive potential effects. The magnitude order of  $\alpha$  was determined by finding the point where the iterative error and the discretization errors become comparable. Time step,  $\Delta t$ , is properly determined so that the iterative schemes converged within a designated number of iterations, while the resulting iterative error does not reach the discretization error. We set  $\Delta t$  to be a certain value so that the magnitude order of the iterative error,  $\|r_i^{L+1,K} - r_i^L\|$  lies between the length scale of particle diameter and an order below. Total clustering time of the particle clusters,  $T$ , was iteratively estimated by varying main two parameters, initial guess of clustering time,  $T_i$  and the number of iterations. Estimated clustering time,  $T_e$ , was calculated by  $T_e = \sum_{i=1}^N \Delta t$

and compared with  $T_i$ . Guessing  $T_i$  and  $N$  were attempted until  $t_r = \frac{T_e - T_i}{T_i}$  (the error between initial guess of clustering time and estimated clustering time) becomes less than 0.01. After this condition was satisfied,  $T$  was assigned as  $T_i$ . After the creation of droplets on the surface from a printing head, it was assumed that the particles in the droplets are initially, randomly dispersed.  $N$  (number of particles in a droplet) sets of three variables in spherical coordinate systems,  $\rho, \theta, \varphi$  were randomly generated and  $x, y, z$  were calculated from the sets. The iterative schemes were designed to be terminated when the average distance between particles was calculated to be less than the particle diameter. Details of the iterative solution schemes, computational algorithms, calculation of total clustering time and determination of the distribution of initial particle displacement are available in supporting information. For calculation, a commercial software, MATLAB R2011a was used for coding and the simulations.

### 4. Results

As observed in Fig. 3, in all cases, silica micro particles and polystyrene micro particles were clustered and formed hemispherical-shaped particle assemblies. However, gold nanoparticles were clustered only if the number of the particles,  $N$ , is over 330 as shown in Fig. 4 and then formed hemisphere-shaped assemblies as similar to silica/polystyrene micro particle cases. Otherwise, the particles were randomly dispersed without clustering.

### 5. Discussion

In order to interpret the drying behaviors, a computational method was used to estimate the particle clustering time at given parameters as described in the previous section. For each material, the magnitude order of  $\alpha$  was determined iteratively by running a few sample simulations, to find a point where the estimated total clustering time was consistent with experimentally observed evaporation time of the suspension droplets. For example, if the clustering of the particles was calculated to be smaller than the evaporation of the

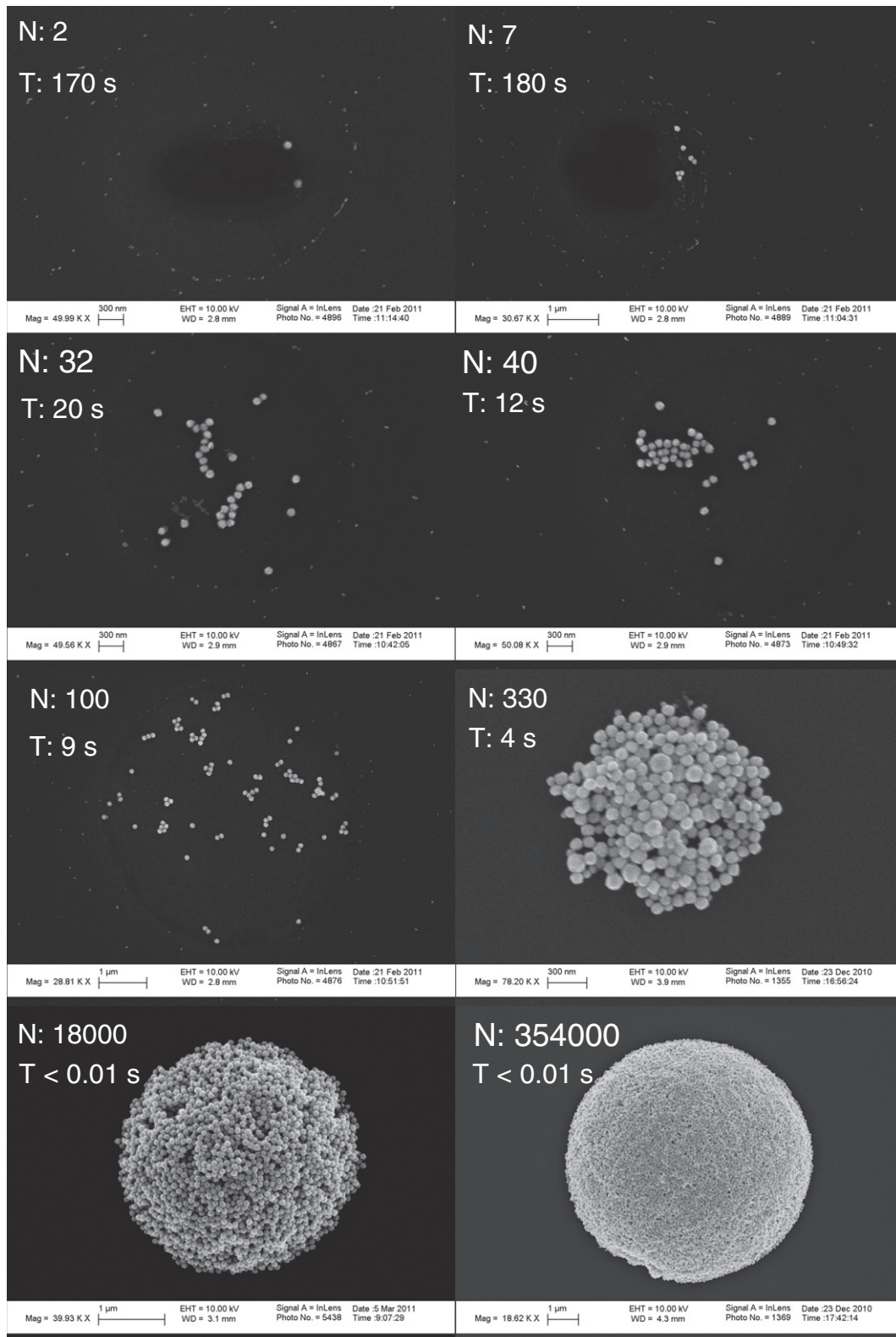


**Fig. 3.** SEM views of microparticle (diameter  $\sim 0.1 \mu\text{m}$ ) clusters. N corresponds to observed (or estimated) number of particles. T corresponds to estimated clustering time of each particle assembly. a. Silica microsphere (diameter  $\sim 1 \mu\text{m}$ ) clusters. b. Polystyrene microsphere (diameter  $\sim 0.5 \mu\text{m}$ ) clusters. The number of particles, N, was either counted from SEM images of assemblies, or estimated by assuming hemisphere geometries and complete packing cases where packing ratio was assumed to be 0.707.

droplets,  $\alpha$  was set in a way that the evaporation time of droplets was above the computed total clustering time. However, in the regime where complete clustering and dispersion of the particles co-existed was found for certain material in Fig. 4a,  $\alpha$  was set in a way that the

evaporation time of the droplets lies within the range of the total clustering time for each number of particles.

Parameters for the computations were obtained by the method in Section 3 and summarized in Table 1. Variation of  $\alpha$  with different

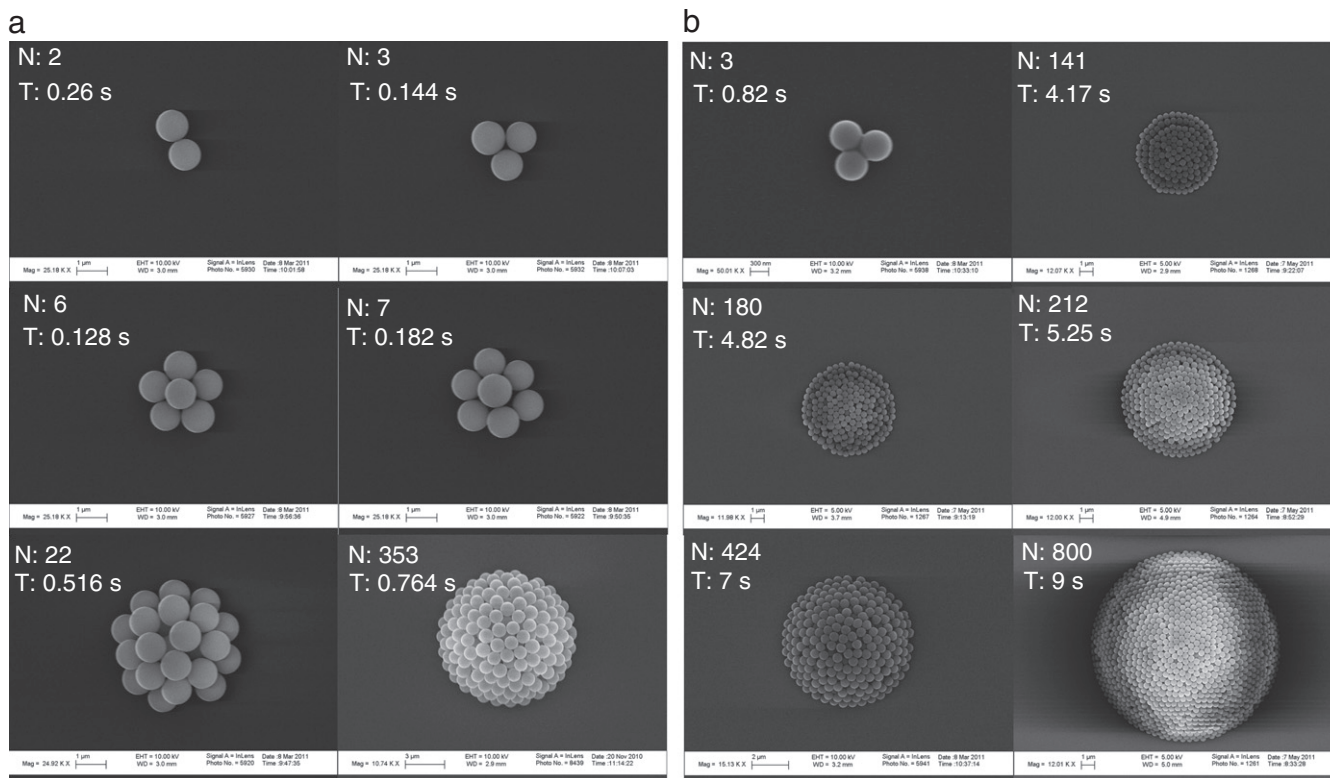


**Fig. 4.** SEM views of gold nanoparticle (diameter  $\sim 0.1 \mu\text{m}$ ) clusters  $N$  corresponds to observed (or estimated) number of particles.  $T$  corresponds to estimated clustering time of each particle assembly.

materials demonstrates that particle-to-particle interaction varies with different materials. It is consistent with general observation that electrostatically more repulsive particles such as PS microparticles or Au nanoparticles show smaller alpha value because stronger, long-range repulsive force trades-off the attractive forces. In general, metallic nanoparticles such as Au nanoparticles are suspended in solvent with ligand-capping [52–55] to prevent aggregation of the particles. The initial state of the suspension-droplet of the Au nanoparticles is designed to be equilibrium. As the droplet evaporates, the overall inter-particle attraction decreases because the hydrodynamic attraction decays as the medium disappears. After final drying, the particles stay dispersed if the repulsive effect outdoes the attraction effect. In case of PS microspheres, the particles are slightly negatively charged without ligand-capping and the repulsive effect is smaller than Au NP particles, but still higher than silica microparticles due to the electrostatic repulsion. Silica microparticles are die-electric and show smaller repulsive effects than other particles. Smaller size-particles may increase the long-range interaction such as van der Waals force, but surface charge is more crucial parameter.

By analyzing the displacement of the particles, the computed clustering time and experimentally-observed evaporation time of the suspension droplets, the particle clustering behavior in evaporative self-assembly were interpreted. The initial displacement of the particles, computed final displacement of particles and center of mass of total particle systems were calculated according to the number of particles in the systems. They are summarized in Table 2.

**Table 1**  
Summary of parameters used for computations.

	Time step ( $\Delta t$ , s)	Alpha ( $\alpha$ )
Sil silica microparticle (d: $1 \mu\text{m}$ )	$10^{-3}$	$10^{-12}$
G gold nanoparticle (d: $0.1 \mu\text{m}$ )	$10^{-2}$	$10^{-16}$
PS microparticle (d: $0.5 \mu\text{m}$ )	$5 \times 10^{-4}$	$10^{-13}$

As verified in Table 2, in silica particle cases, at given potential, all particles in the given system were calculated to be clustered to the center of mass of the system for all numbers of the particles. In Fig. 2, after the completion of evaporation, the centering of the particle cluster to initial droplet contact-line was observed. The centering was reproducible with all experiments with random distribution of initial particle displacements. These computational and experimental results suggest that the clustering rate of the particles is equal or higher than the evaporative rate of the liquid medium. Otherwise, the particle clusters will be deposited at different locations (other than the center of the droplet contact line). If the particle-to-particle clustering rate does not reach the evaporative rate of the liquid medium, evaporative force of liquid medium overwhelms the particle-to-particle interactive forces and particles are dispersed after the completion of the evaporation as shown in gold nanoparticles in Fig. 4. In this case, we can approximate that the particles are carried by the fluid and apply the conventional hydrodynamic models to explain the transportation of the particles. It is speculated that the clustering of the particles is completed prior to the evaporation of the droplets and evaporation of the droplet drives the already formed, cluster to the center of droplet contact-line. This hypothesis can explain the reproducibility of complete centering of the particle clusters, however, more experimental results are to be provided for verification. For future work, by using advanced optics, thorough examination of particle movement and medium-evaporation is expected to verify the hypothesis.

Interpretation of numerous, evaporative self-assembly-based phenomenon, such as convective assembly [5,14,15,44–49], coffee-ring effect [14,39–42,56–59], or rapid self-assembly on hydrophobic surfaces [7,14,17,60–63] can be assisted by using the microscopic models. For instance, in the coffee-ring effect, a number of previous works [14,39–42,56–59] have attempted to explain the particle-pinning at the droplet contact line on the substrate by applying hydrodynamic models. In those approaches, crude assumptions were made to validate mathematical models, and have resulted in incomplete description of the

**Table 2**

Calculated initial particle displacement, final displacement and center of mass of the particle systems with respect to coordinate systems as defined in Fig. 3 a for N = 2, 3, 4, 5, 6. (Unit:  $\mu\text{m}$ ).

Number of particles	Initial displacement			Computed final displacement			Center of mass		
2	17.87	-4.89	34.31	12.52	-3.26	54.73	12.38	-3.22	55.28
	6.89	-1.55	76.24	12.24	-3.17	55.81			
3	-32.72	-98.74	15.54	3.22	-38.95	36.99	3.31	-38.79	37.03
	11.66	-9.54	32.38	3.30	-38.64	36.92			
	30.98	-8.10	63.18	3.41	-38.79	37.20			
4	0.03	0.01	2.13	4.09	9.55	74.86	4.10	9.68	75.08
	-7.03	2.65	8.79	3.84	9.77	75.05			
	3.21	2.54	6.33	4.14	9.90	75.10			
	5.43	-1.33	12.78	4.30	9.57	75.27			
5	17.34	-4.90	28.64	-10.35	19.41	34.81	-10.71	19.53	34.80
	-2.44	-1.25	56.48	-10.76	19.37	35.13			
	1.69	0.67	13.38	-10.87	19.28	34.56			
	0.89	9.31	15.93	-10.60	19.79	34.58			
	-71.05	93.81	59.55	-10.97	19.78	34.91			
6	10.06	-54.48	77.37	4.65	-8.35	39.85	4.75	-7.93	39.72
	-0.4	-1.79	19.03	4.31	-7.87	39.64			
	59.81	-41.35	70.06	5.19	-7.94	39.79			
	11.57	-9.46	0.00	4.84	-8.1	39.32			
	-46.08	78.87	5.77	4.78	-7.50	39.59			
	-6.46	-19.35	66.11	4.72	-7.81	40.16			

phenomena. However, if microscopic models are applied to three-phase contact-line, it is interpreted that the initial particle-pinning on the substrate is driven by particle-to-substrate and particle-to-particle attractive force. The particle-substrate attractive force,  $\psi_i^{pf}$ , is maximized at the edge of the droplet where the thickness of the medium is minimal. Drag-effect of the particles is minimized and  $\psi_i^{pf}$  drives the particle-pinning at the edge of the three-phase contact line. This interpretation is also analogous with the claim of Shen's work [57] that the lower limiting size of a coffee ring is dependent on the time scale competition between the liquid evaporation and the movement of suspended particles. When the liquid evaporates much faster than the particle movement near a three-phase contact line, a coffee ring is not formed. Instead, these particles will disperse on a surface upon the completion of liquid medium-evaporation. In our work, instead of coffee-rings, high aspect ratio-particle clusters were formed when the clustering rate of the particles exceeds the evaporative rate of the liquid. Dominance of particle-to-particle interaction over the "hydrodynamic effect" of evaporating medium is a necessary condition to create particle clusters in evaporative self-assembly. In the same way, the assembly of the colloids in convective assembly can be interpreted without using unknown "solvent-evaporative term" as appeared in earlier works [5,15,29,46]. Particle-to-particle interaction forces are maximized where the thickness of the medium is thinnest. From that point, evaporative self-assembly of the particles initiates and propagates to the rest of the region. Also, particle-to-particle interactions allow the interpretation of particle clustering behavior in multi-phase flows, which conventional hydrodynamic models are incapable of.

In Fig. 5, particle clustering times were computed for 10 different sets of 2-silica particle system and compared with the evaporation time of the droplets. It shows that the particle clustering time is smaller than the evaporation time of the droplets for all randomly distributed initial particle displacements. Clustering behaviors of the particles were examined by computing inter-particle spacing with respect to time. When two particles are clustered, the spacing decreases linearly until the completion of the clustering. The slope of the decrease becomes steeper as the number of particles increases, because the total sum of particle interactive forces increases and the total acceleration of the system also increases as well. The trend of total clustering time with the number of particles was studied in-depth.

As shown in Figs. 6, 7, the trend for clustering time versus the number of the particles varies with materials. The range of the

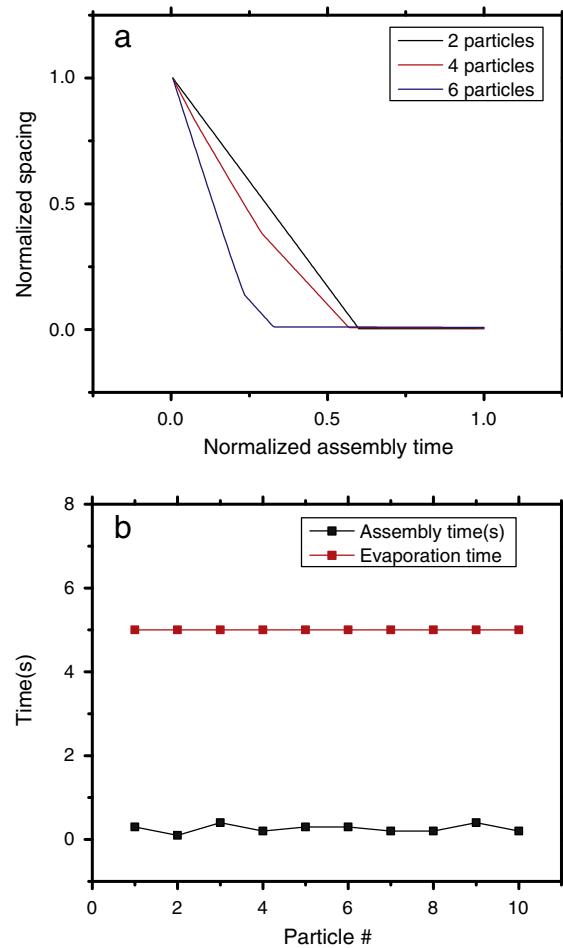


**Fig. 5.** a. Computed, normalized average inter-particle distance with respect to normalized assembly time. 2 particles, 4 particles and 6 particle-silica particle systems are computed. Normalized spacing refers to (inter-particle distance at given moment)/(initial inter-particle distance) and normalized assembly time refers to (time at given moment)/(total assembly time). b. Computed, particle clustering time of 10 different sets of 2-particle systems and comparison with the experimentally observed-evaporation time of the droplet.

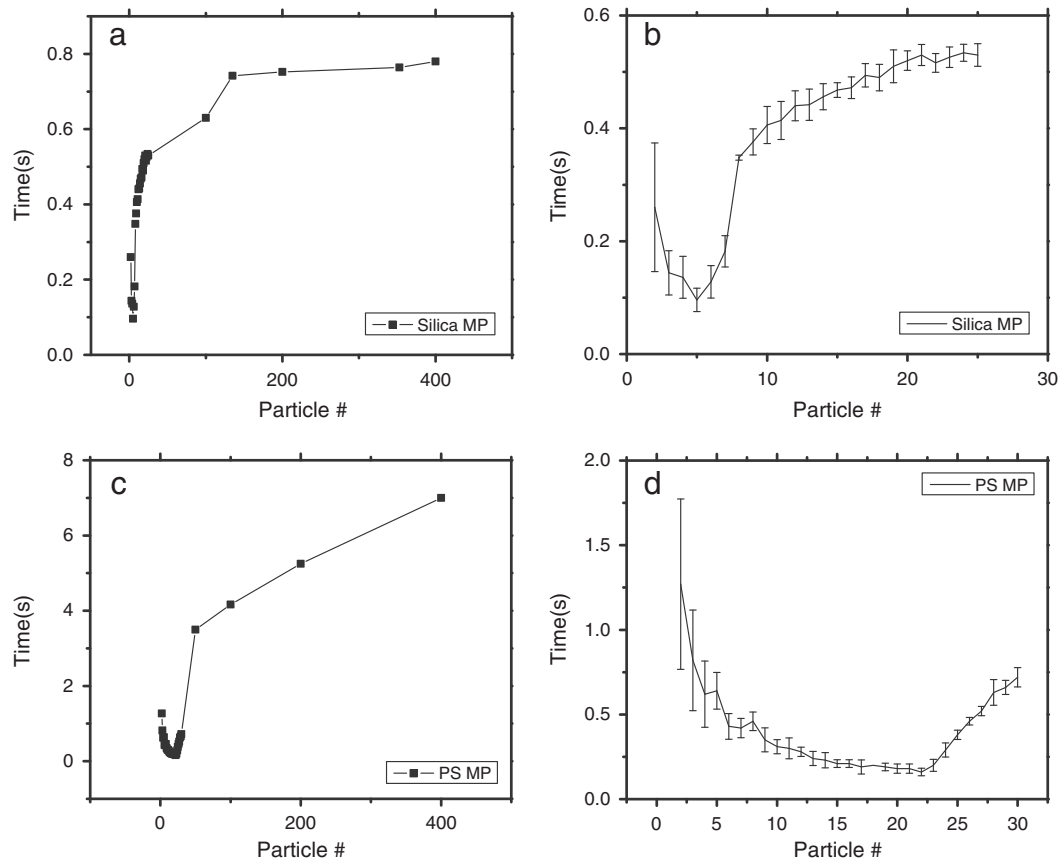


**Fig. 6.** a–d. Particle clustering time with respect to the number of microparticles. The dot indicates where experiments were actually performed. The range of particle number was from 2 to 400. The error bar shows the variation of clustering time by the initial random distribution of 5 different sets of 2 particle systems. a. Silica micro particles, b. a zoomed part of a graph near the turning point of the slope of (time)/(particle). c. Polystyrene micro particles. d. A zoomed part of c graph near the turning point of the slope of (time)/(particle).

number of the particles is from 2 to 400. In both silica and polystyrene cases, all clustering times fall within the evaporation time of the droplet. The regime of low particle number is defined as the range of the particles from 2 to the particle number where the clustering time is minimum. The regime of high particle number is defined as the range of the particles from the particle number where the clustering time is minimum to the last number, 400. In the regime of low particle numbers, the clustering time decreases as the number of the particles increases, due to the increase of total sum of particle interaction forces. However, if the number of the particles exceeds a critical value, the clustering time increases. In order to understand this result, a scaling analysis of the governing Eq. (1) was performed by non-dimensionalization:

$$\left(\frac{MU^2}{L}\right)m_i\ddot{r}_i^* + \left(\frac{MU^2}{L}\right)c_i\dot{r}_i^* = \left(\frac{N-1}{L}\right)\sum_{j \neq i}^{N_p} \left(\alpha \|r_i^* - r_j^*\|^{-1}\right)n_{ij} \quad (13)$$

where \* represents dimensionless parameter,  $M$  is a characteristic mass of the particle,  $U$  is a characteristic velocity of the particle,  $L$  is a characteristic length of the particle and  $N$  is the number of particles in the system. By dividing the denominator of the first term, the equation becomes (14)

$$\underbrace{m_i\ddot{r}_i^* + \left(\frac{1}{U}\right)c_i\dot{r}_i^*}_{\text{Drag}} = \underbrace{\left(\frac{N-1}{MU^2}\right)\sum_{j \neq i}^{N_p} \left(\alpha \|r_i^* - r_j^*\|^{-1}\right)n_{ij}}_{\text{Particle-particle interaction}} \quad (14)$$

The acceleration of the particle is determined by the competition between drag term and particle-interaction term. The drag term scales with  $\frac{1}{U}$  and the particle-interaction term scales with  $\frac{(N-1)}{MU^2}$ . In the regime of low particle number, as the particle number increases,

the particle-interaction term increases and the drag term does not change significantly, because the velocity does not vary drastically by adding a few more particles to the existing system. However, in the regime of high particle number, as the particle number increases, the velocity of the particle increases and the drag term becomes more dominant than the particle-interaction term. As a result, the acceleration of the particles decreases and the total particle clustering time increases. However, in case of gold nanoparticle, the regime of high particle number was not observed and the clustering time decreases as the particle number increases. The critical number of the particles is defined as a corresponding particle number where the evaporation time of the droplet is equal to the particle clustering time. As shown in Fig. 4, there exist a critical number of gold nanoparticles (~300) where the cluster starts being formed. If the particle number is below the critical number, the particles are not clustered and randomly dispersed. In other words, if the particle clustering time at a certain particle number is calculated to be longer than the evaporation time of the droplet, the clustering is not achieved and the particles will be randomly dispersed. However, if the particle-assembly time at a certain particle number is calculated to be shorter than the evaporation time of the droplet, the clustering is achieved.

The simulation results show that a particle-based computational method allows efficient interpretation of evaporative self-assembly of micro particles in small scale suspension droplets.

## 6. Conclusions

Evaporative self-assembly of micro particles in picoliter droplets was achieved and monitored by a droplet-dispensing system for particle suspensions. In order to interpret the assembly behavior, a particle-based computational method was developed. The experimental

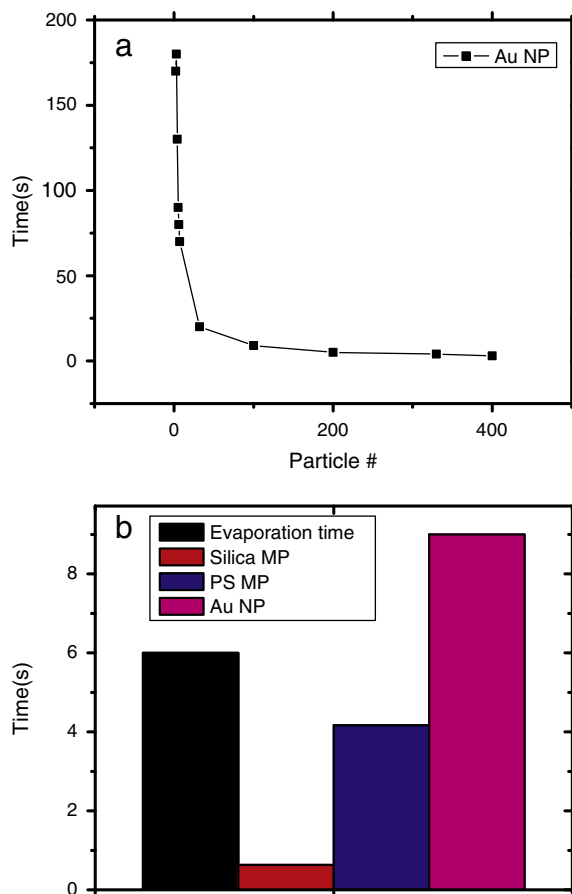


**Fig. 7.** a. Particle clustering time with respect to the number of gold nanoparticles. b. Comparison of particle clustering time with evaporation time of the droplet in case the particle number is fixed to be 100 for all types of particles.

and computational results suggest that the competition between the time scale for particle-to-particle clustering and evaporative rate of liquid medium, determines the final morphologies of micro particle assemblies. It is also shown that the particle-based computational method allows for proper interpretation of evaporative self-assembly of micro particles in small scale suspension droplets.

### Acknowledgment

This work was supported by a grant (2009K000069) from the Center for Nanoscale Mechatronics & Manufacturing (CNMM), one of the 21st Century Frontier Research Programs, which are supported by Ministry of Education, Science and Technology, Korea. We also acknowledge technical support from Jeffrey Clarkson for measuring light intensity of optical microscope in Berkeley Marvell Nanofabrication Laboratory. S. Choi also gives thanks for his graduate fellowship from Samsung Scholarship Foundation.

### Appendix A. Supplementary data

Detailed calculations for scaling analysis and pressure loss calculation based on fluid mechanics, and estimating the number of the nanoparticle clusters,  $n$ , in 30  $\mu\text{m}$  diameter clusters are available in supporting information. Supplementary data to this article can be found online at <http://dx.doi.org/10.1016/j.tsf.2013.04.047>.

### References

- [1] H. Miguez, S.M. Yang, G.A. Ozin, *Langmuir* 19 (2003) 3479.
- [2] T. Yamasaki, T. Tsutsui, *Appl. Phys. Lett.* 72 (1998) 1957.
- [3] Y. Zhao, I. Avrutsky, *Opt. Lett.* 24 (1999) 817.
- [4] N. Bowden, A. Terfort, J. Carbeck, G.M. Whitesides, *Science* 276 (1997) 233.
- [5] N.D. Denkov, O.D. Velev, P.A. Kralchevsky, I.B. Ivanov, H. Yoshimura, K. Nagayama, *Nature* 361 (1993) 26.
- [6] E. Rabani, D.R. Reichman, P.L. Geissler, L.E. Brus, *Nature* 426 (2003) 271.
- [7] R. Mukhopadhyay, O. Al-Hanbali, S. Pillai, A.G. Hemmersam, R.L. Meyer, A.C. Hunter, K.J. Rutt, F. Besenbacher, S.M. Moghimi, P. Kingshott, *J. Am. Chem. Soc.* 129 (2007) 13390.
- [8] D. Qin, Y. Xia, B. Xu, H. Yang, C. Zhu, G.M. Whitesides, *Adv. Mater.* 11 (1999) 1433.
- [9] Y. Masuda, W.S. Seo, K. Koumoto, *Thin Solid Films* 382 (2001) 183.
- [10] Y. Masuda, K. Tomimoto, K. Koumoto, *Langmuir* 19 (2003) 5179.
- [11] Y. Masuda, T. Itoh, K. Koumoto, *Langmuir* 21 (2005) 4478.
- [12] Y. Masuda, T. Itoh, M. Itoh, K. Koumoto, *Langmuir* 20 (2004) 5588.
- [13] Y. Masuda, M. Itoh, T. Yonezawa, K. Koumoto, *Langmuir* 18 (2002) 4155.
- [14] S. Choi, S. Stassi, A.P. Pisano, T.I. Zohdi, *Langmuir* 26 (2010) 11690.
- [15] S. Choi, I. Park, Z. Hao, H.-Y.N. Holman, A.P. Pisano, T.I. Zohdi, *Langmuir* 26 (2010) 4661.
- [16] S. Choi, A. Jamshidi, T.J. Seok, M.C. Wu, T.I. Zohdi, A.P. Pisano, *Langmuir* 28 (2012) 3102.
- [17] Y. Masuda, T. Itoh, K. Koumoto, *Adv. Mater.* 17 (2005) 841.
- [18] H. Miguez, S.M. Yang, G.A. Ozin, *Appl. Phys. Lett.* 81 (2002) 2493.
- [19] J.R. Savage, D.W. Blair, A.J. Levine, R.A. Guyer, A.D. Dinsmore, *Science* 314 (2006) 795.
- [20] O. Kletenik-Edelman, E. Ploshnik, A. Salant, R. Shenhar, U. Banin, E. Rabani, *J. Phys. Chem. B* 112 (2008) 4498.
- [21] A. Lomakin, N. Asherie, G.B. Benedek, *Proc. Natl. Acad. Sci.* 100 (2003) 10254.
- [22] C.B. Murray, *Science* 324 (2009) 1276.
- [23] J. Park, H. Zheng, W.C. Lee, P.L. Geissler, E. Rabani, A.P. Alivisatos, *ACS Nano* 6 (2012) 2078.
- [24] P.S. Richard, *J. Phys.* 19 (2007) 033101.
- [25] E.V. Shevchenko, D.V. Talapin, N.A. Kotov, S. O'Brien, C.B. Murray, *Nature* 439 (2006) 55.
- [26] P.R.T. Wolde, D. Frenkel, *Science* 277 (1997) 1975.
- [27] G. Yosef, E. Rabani, *J. Phys. Chem. B* 110 (2006) 20965.
- [28] X. Zhang, T. Imae, *J. Phys. Chem. C* 113 (2009) 5947.
- [29] A.S. Dimitrov, K. Nagayama, *Langmuir* 12 (1996) 1303.
- [30] P.A. Kralchevsky, N.D. Denkov, *Curr. Opin. Colloid Interface* 6 (2001) 383.
- [31] P.A. Kralchevsky, K. Nagayama, *Adv. Colloid Interf.* 85 (2000) 145.
- [32] A. Donev, S. Torquato, F.H. Stillinger, *J. Comput. Phys.* 202 (2005) 737.
- [33] J. Duran, *Sands, powders and grains, An Introduction to the Physics of Granular Matter*, Springer Verlag, 1997.
- [34] T.A.S. Poschel, *Computational Granular Dynamics*, Springer Verlag, 2004. (T).
- [35] T. Zohdi, *Arch. Comput. Meth. Eng.* 17 (2010) 109.
- [36] T.I. Zohdi, *Dynamics of charged particulate systems, Modeling, Theory and Computation*, Springer-Verlag, 2012.
- [37] R. Roscoe, *Br. J. Appl. Phys.* 3 (1952) 267.
- [38] H. Hu, R.G. Larson, *J. Phys. Chem. B* 110 (2006) 7090.
- [39] B.J. Fischer, *Langmuir* 18 (2001) 60.
- [40] V.N. Truskett, K.J. Stebe, *Langmuir* 19 (2003) 8271.
- [41] R.D. Deegan, O. Bakajin, T.F. Dupont, G. Huber, S.R. Nagel, T.A. Witten, *Nature* 389 (1997) 827.
- [42] R.D. Deegan, *Phys. Rev. E* 61 (2000) 475.
- [43] R. Bhardwaj, X. Fang, P. Somasundaran, D. Attinger, *Langmuir* 26 (2010) 7833.
- [44] P. Born, S. Blum, A. Munoz, T. Kraus, *Langmuir* 27 (2011) 8621.
- [45] N.-G. Cha, Y. Echegoyen, T.-H. Kim, J.-G. Park, A.A. Busnaina, *Langmuir* 25 (2009) 11375.
- [46] N. Denkov, O. Velev, P. Kralchevsky, I. Ivanov, H. Yoshimura, K. Nagayama, *Langmuir* 8 (1992) 3183.
- [47] E. Kim, Y. Xia, G.M. Whitesides, *Adv. Mater.* 8 (1996) 245.
- [48] Y. Mino, S. Watanabe, M.T. Miyahara, *Langmuir* 27 (2011) 5290.
- [49] E.C.H. Ng, K.M. Chin, C.C. Wong, *Langmuir* 27 (2011) 2244.
- [50] H. Hu, R.G. Larson, *Langmuir* 21 (2005) 3963.
- [51] S. Hlushak, A. Trokhymchuk, *Condens. Matter Phys.* 15 (2012).
- [52] K. Lee, A.N. Sathyagal, A.V. McCormick, *Colloids Surf. A* 144 (1998) 115.
- [53] T. Kim, K. Lee, M.-S. Gong, S.-W. Joo, *Langmuir* 21 (2005) 9524.
- [54] H. Tan, B. Liu, Y. Chen, *Plasmonics* (2012) 1.
- [55] M.K. Chow, C.F. Zukoski, *J. Colloid Interface Sci.* 165 (1994) 97.
- [56] H.B. Eral, D.M. Augustine, M.H.G. Duits, F. Mugele, *Soft Matter* 7 (2011) 4954.
- [57] X. Shen, C.-M. Ho, T.-S. Wong, *J. Phys. Chem. B* 114 (2010) 5269.
- [58] K. Uno, K. Hayashi, T. Hayashi, K. Ito, H. Kitano, *Colloid Polym. Sci.* 276 (1998) 810.
- [59] B.M. Weon, J.H. Je, *Phys. Rev. E* 82 (2010) 015305.
- [60] W. Han, M. Byun, Z. Lin, *J. Mater. Chem.* 21 (2011) 16968.
- [61] J. Park, J. Moon, H. Shin, D. Wang, M. Park, *J. Colloid Interf. Sci.* 298 (2006) 713.
- [62] J. Xu, J. Xia, S.W. Hong, Z. Lin, F. Qiu, Y. Yang, *Phys. Rev. Lett.* 96 (2006) 066104.
- [63] J. Xu, J. Xia, Z. Lin, *Angew. Chem. Int. Edit* 46 (2007) 1860.